J. Fluid Mech. (2008), *vol.* 600, *pp.* 271–289.
doi:10.1017/S0022112008000529 Printed in the United Kingdom

Stability limits of unsteady open capillary channel flow

ALEKSANDER GRAH, DENNIS HAAKE, UWE ROSENDAHL, JÖRG KLATTE AND MICHAEL E. DREYER

Center of Applied Space Technology and Microgravity (ZARM), University of Bremen, Am Fallturm, Bremen, D-28359, Germany

(Received 8 August 2007 and in revised form 8 January 2008)

This paper is concerned with steady and unsteady flow rate limitations in open capillary channels under low-gravity conditions. Capillary channels are widely used in Space technology for liquid transportation and positioning, e.g. in fuel tanks and life support systems. The channel observed in this work consists of two parallel plates bounded by free liquid surfaces along the open sides. The capillary forces of the free surfaces prevent leaking of the liquid and gas ingestion into the flow.

In the case of steady stable flow the capillary pressure balances the differential pressure between the liquid and the surrounding constant-pressure gas phase. Increasing the flow rate in small steps causes a decrease of the liquid pressure. A maximum steady flow rate is achieved when the flow rate exceeds a certain limit leading to a collapse of the free surfaces due to the choking effect. In the case of unsteady flow additional dynamic effects take place due to flow rate transition and liquid acceleration. The maximum flow rate is smaller than in the case of steady flow. On the other hand, the choking effect does not necessarily cause surface collapse and stable temporarily choked flow is possible under certain circumstances.

To determine the limiting volumetric flow rate and stable flow dynamic properties, a new stability theory for both steady and unsteady flow is introduced. Subcritical and supercritical (choked) flow regimes are defined. Stability criteria are formulated for each flow type. The steady (subcritical) criterion corresponds to the speed index defined by the limiting longitudinal small-amplitude wave speed, similar to the Mach number. The unsteady (supercritical) criterion for choked flow is defined by a new characteristic number, the dynamic index. It is based on pressure balances and reaches unity at the stability limit.

The unsteady model based on the Bernoulli equation and the mass balance equation is solved numerically for perfectly wetting incompressible liquids. The unsteady model and the stability theory are verified by comparison to results of a sounding rocket experiment (TEXUS 41) on capillary channel flows launched in December 2005 from ESRANGE in north Sweden. For a clear overview of subcritical, supercritical, and unstable flow, parametric studies and stability diagrams are shown and compared to experimental observations.

1. Introduction

Open capillary channels are used in a large number of applications in liquid management in Space, e.g. advanced life support systems, heat pipes and in surface tension tanks of spacecrafts. They create and maintain a flow path between two

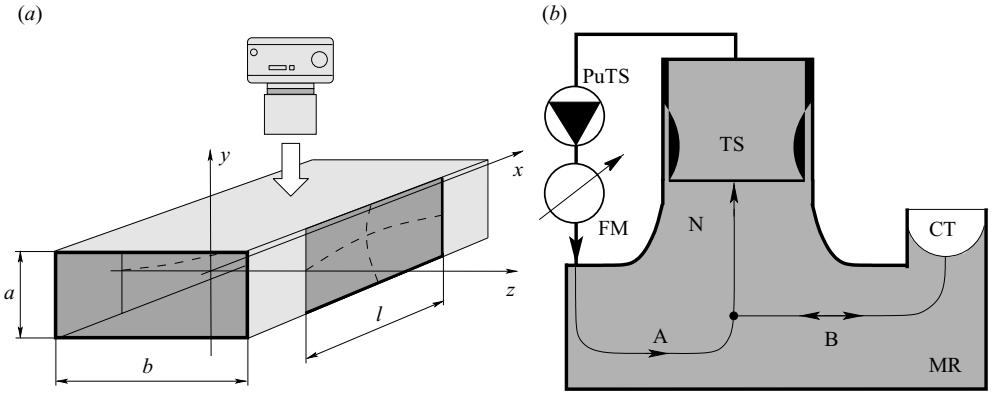

FIGURE 1. (*a*) Capillary channel consisting of two glass plates with two free liquid surfaces on the sides (camera view from top). (*b*) Experimental set-up (TEXUS 41) with the test section TS (capillary channel camera image), compensation tube CT, main reservoir MR, pump PuTS, the flow rate sensor FM and the nozzle N. The main liquid loop is driven by the pump along streamline A. Flow rate changes induce liquid oscillations between TS and CT along streamline B.

variable points along their axis and capture the liquid by capillary forces. Thus, capillary channels are widely used for the transport and positioning of propellants (Jaekle 1991; Srinivasan 2003).

The open capillary channel considered in this work consists of two parallel plates with one free liquid surface on each side, as depicted in figure 1(*a*). For an internal pressure p lower than ambient pressure p_a the free liquid surfaces have a concave shape. The channel is connected to ducts of closed circumference. The main liquid loop is driven by a gear pump, along a streamline a, shown in figure 1(*b*). A secondary flow along streamline B is a consequence of the surface movement and liquid displacement from the channel into the compensation tube and vice versa.

Increasing the pump flow rate Q increases the differential pressure between the liquid and the surrounding constant gas pressure. At a maximum flow rate Q_{max} the free surfaces of the channel collapse and gas ingestion into the liquid occurs. This might cause bubbles in the propellant and degradation of the thruster performance. For technical applications the flow rate must be limited below the maximum value.

The effect of the steady flow rate limitation due to choking has been the subject of a previous paper (Rosendahl, Ohlhoff & Dreyer 2004). In general, choking occurs when the local fluid velocity v reaches the value of the limiting longitudinal small-amplitude wave speed v_{ca} and the capillary *speed index* reaches unity: $S_{ca} \equiv v/v_{ca} = 1$. A steady flow is obtained only for a flow rate below this critical value (subcritical flow).

In this paper the flow limitation theory is revised for steady flow and extended for unsteady conditions. The unsteady effect is defined by a dynamic flow rate increase during a given time period, and causes an additional flow rate limitation. On the other hand, unsteady flow can temporarily be choked but remains stable. Hence the choking effect defines two flow regimes, subcritical and supercritical (choked) flow. The demarcation between these regimes is defined by the speed index, which reaches unity at a critical (choking) point. Stable steady flow is possible in the subcritical regime only and the surfaces collapse at the critical point. Unsteady flow can temporarily reach the supercritical regime, which is mainly influenced by the

Lengths	Velocities	Others	Characteristic numbers
$x = x'/l$	$v_c = \sqrt{2\sigma/(\rho a)}$	$t = t' v_c / l$	$Oh = \sqrt{\rho \nu^2/(2\sigma a)}$
$y = 2y'/a$	$v = v'/v_c$	$A_0 = ab$	$\Lambda = b/a$
$z = 2z'/a$	$v_{ca} = v'_{ca}/v_c$	$A = A'/A_0$	$\tilde{l} = Oh\ l/(4a)$
$k = 2k'/a$		$p = ap'/(2\sigma)$	$Q = Q'/(A_0 v_c)$
$R = 2R'/a$		$h = ah'/2$	$\delta = \Delta Q/\Delta t$
$R_{1,2} = 2R'_{1,2}/a$		$\Gamma = a/(2l)$	
$l_0 = l'_0/l$		$Re = 2av'/\nu$	

TABLE 1. Scaled variables and characteristic numbers.

choking effect. The stability in the supercritical flow regime can be explained by a pressure balance at the liquid surface.

In the studies an unsteady mathematical model is used (one-dimensional approach). The model is based on the mass balance equation, the Bernoulli equation, the Gauss–Laplace equation and the appropriate boundary conditions. To solve the equations second-order finite difference approximations are applied. For the integration of the differential-algebraic equation system a linearly implicit method is used. The numerical solutions are verified by comparison to experimental measurement and coincide well.

This paper is organized in five sections. In § 2 the unsteady flow model for the open capillary channel is formulated. Based on the model, § 3 formulates an augmented theory for the steady and unsteady flow rate limitation for open capillary channels. The reliability of the model is demonstrated by comparison to experimental results and numerical studies in § 4. Steady and dynamic flow limitation effects are discussed, based on the speed index S_{ca} and a new characteristic number, the *dynamic index* D. The accuracy of the stability prediction is demonstrated by comparison to experimentally observed flow regimes. The paper is summarized in § 5.

2. The model

The model considers unsteady liquid flow through an open parallel plate channel, as shown in figure 1(*a*). The gap distance, the width of the plates and the length of the open section are denoted a, b and l, respectively. The origin of the coordinate system is located at the centre of the inlet cross-section. We assume an incompressible, perfectly wetting Newtonian liquid and isothermal conditions. The maximum Reynolds number Re (table 1) in the channel is lower than 10^3 and therefore the flow is assumed to be laminar. The unsteady effect is induced by increasing the pump flow rate Q. The pump is located at the outlet of the capillary channel, as shown in figure 1(*b*). It is assumed that the velocity component in the flow direction x is significantly larger than in the lateral (y, z) directions, and that the cross-section changes are sufficiently small. Hence the flow along the channel axis x may be considered as one-dimensional. Owing to the low gravity environment, the hydrostatic pressure distribution over the channel cross-section is negligible, and the pressure p over the flow cross-section area A may be considered as constant.

2.1. *Scaling*

Dimensionless quantities were used to solve the model equations. The scaling quantities are given in table 1. The x-axis is scaled with the channel length l, all other lengths with $a/2$. Velocities are scaled by the characteristic velocity $v_c = \sqrt{2\sigma/(\rho a)}$ where σ is the surface tension and ρ the density of the liquid. The time is scaled by

v_c and the channel length l; the cross-sectional area A by the inlet value $A_0 = ab$. The pressure is scaled with a characteristic capillary pressure $2\sigma/a$. The flow is considered to be one-dimensional along the channel axis x and is characterized by the mean velocity v and the liquid pressure p. Furthermore the dimensionless channel length

$$\tilde{l} = \frac{Oh\, l}{4a} \tag{2.1}$$

is introduced, a common scaling of frictional duct flows. The Ohnesorge number is

$$Oh = \sqrt{\frac{\rho v^2}{2\sigma a}} = \frac{2}{Re_c} \text{ with } Re_c = \frac{2a v_c}{\nu}. \tag{2.2}$$

The Ohnesorge number is inversely proportional to the Reynolds number based on the characteristic velocity v_c; ν denotes the kinematic viscosity. The aspect ratio is

$$\Lambda = \frac{b}{a}. \tag{2.3}$$

2.2. *Governing equations*

The dimensionless governing equations are the unsteady mass balance equation

$$-\partial_t A = v\partial_x A + A\partial_x v \tag{2.4}$$

and the unsteady Bernoulli equation (White 1986) with a viscous pressure loss term in the flow direction and differentiated with respect to the x-coordinate

$$-\partial_t v = \partial_x p + v\partial_x v + \partial_x w_f \tag{2.5}$$

where $\partial_t = \partial/\partial t$ and $\partial_x = \partial/\partial x$ are the temporal and spatial derivatives. Since the viscosity of the gas is significantly smaller the tangential stresses at the free surface are negligible and the surrounding gas phase may be regarded as passive. Thus, the capillary pressure $p - p_a$ is directly related to the curvature of the liquid surface. It can be determined by the Gauss–Laplace equation (Landau & Lifschitz 1959)

$$p - p_a = -h = -\left(\frac{1}{R_1} + \frac{1}{R_2}\right). \tag{2.6}$$

R_1 and R_2 are the principal radii and $h/2$ the mean curvature of the liquid surface. Since the ambient pressure p_a is constant, the pressure gradient in equation (2.5) becomes

$$\partial_x p = -\partial_x h. \tag{2.7}$$

The viscous pressure loss w_f is based on both laminar pressure loss w_{pf} of a fully developed flow profile and additional pressure loss w_{Sf} due to development of the velocity profile in the entrance region. For one-dimensional steady flow with constant cross-section the pressure loss yields

$$\partial_x w_f = \frac{K_f Oh}{8a} l v = \frac{K_f}{2}\tilde{l} v, \tag{2.8}$$

with the pressure loss factor

$$K_f = K_{pf} + 16\hat{K}_{Sf}, \tag{2.9}$$

and $K_{pf} = 96$ for parallel plates (White 1986). Assuming an initial plug flow for the additional pressure loss due to the profile change, a pressure-drop function K_{Sf} for

parallel plates from Sparrow & Lin (1964) is applied. In differential form it is

$$\hat{K}_{Sf} = \frac{\mathrm{d}K_{Sf}(\hat{x})}{\mathrm{d}\hat{x}} \tag{2.10}$$

and depends on the coordinate $\hat{x} = 4\nu x'/(a^2 v') + s_0$. This term contributes only within the entrance length l_e where the profile changes. Therefore the velocity profile at the channel inlet is partly developed and deviates from the assumed plug profile. To consider this entrance velocity profile, the coordinate x in equation (2.10) is shifted by

$$s_0 = \frac{LOh}{2v_0 A_0}, \tag{2.11}$$

where v_0 is the velocity and A_0 is the cross-section at the channel inlet. The entrance factor L is defined by the nozzle in the flow path before the channel entrance, as shown in figure 1 and was calculated by three-dimensional numerical simulations using commercial software (the parameter values are given in § 4.1). The pressure loss effects are assumed to be significant for the initial and final steady states but of minor importance for the dynamic behaviour of the flow. Nevertheless the pressure loss effects are considered to maintain compatibility with the model of Rosendahl *et al.* (2004).

The surface model of Rosendahl *et al.* (2004) is used for the connection of the cross-sectional area A to the capillary pressure p or curvature $h/2$. It assumes symmetry with respect to the planes $y = 0$ and $z = 0$ in figure 1. The contour k represents the innermost surface position in the symmetry plane $y = 0$ (surface profile). The model defines h and A as a function of k and its derivatives with respect to x, $\partial_x k = \partial k/\partial x$ and $\partial_{xx} k = \partial^2 k/\partial x^2$. The Gauss–Laplace equation (2.6) can be expressed as a function of the free surface contour k only:

$$h(x) = \frac{1}{R_1} + \frac{1}{R_2} = \frac{1}{R_1} + \frac{\Gamma^2 \partial_{xx} k}{\left[1 + \Gamma^2 (\partial_x k)^2\right]^{3/2}}, \quad \Gamma = a/(2l). \tag{2.12}$$

The pressure and the curvature in the principal plane (y, z^*) are assumed to be constant. The surface is a segment of a circle with radius R_1 that may be derived using the geometrical relations of figure 2:

$$R_1 = \frac{1 + d^{*2}}{2d^*}, \qquad d^* = d\left[1 + \Gamma^2 (\partial_x k)^2\right]^{1/2}, \qquad d = \Lambda - k. \tag{2.13}$$

The radius R_1 may change between infinity (plane surface) and unity (maximum curvature). When the liquid separates from the edges of the channel, the free surface moves inwards between the parallel plates and the cross-sectional area decreases further. Since the contact angle between the liquid and the solid is zero, the radius of curvature is half the plate distance apart, $R_1 = 1$. For the pinned and separated conditions we obtain

$$R_1 = \begin{cases} \dfrac{1 + (\Lambda - k)^2 \left[1 + \Gamma^2 (\partial_x k)^2\right]}{2(\Lambda - k)\left[1 + \Gamma^2 (\partial_x k)^2\right]^{1/2}} & \text{for} \quad k \geqslant \Lambda - \left[1 + \Gamma^2 (\partial_x k)^2\right]^{-1/2} \\ 1 & \text{for} \quad k < \Lambda - \left[1 + \Gamma^2 (\partial_x k)^2\right]^{-1/2}. \end{cases} \tag{2.14}$$

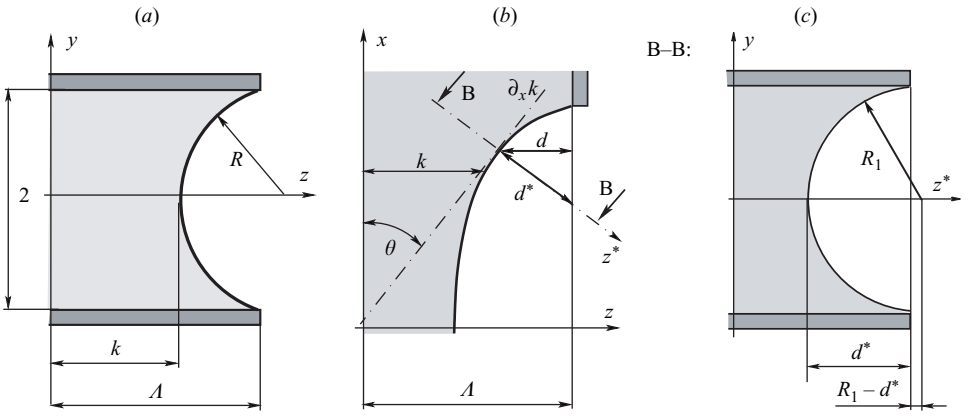

FIGURE 2. (*a*) Cross-section of the channel in the (y, z)-plane; the radius R is visible. (*b*) Cut through the (x, z)-plane; flow direction is upwards. (*c*) Cut through the tilted (y, z^*)-plane; the first principal radius R_1 is visible. The liquid is shown grey.

The cross-sectional area A (figure 2) is defined as a function of the profile contour k:

$$A(k) = \begin{cases} 1 - \dfrac{R^2}{2\Lambda}\arcsin\dfrac{1}{R} + \dfrac{1}{2\Lambda}(R - \Lambda + k);\, R = \dfrac{1 + (\Lambda - k)^2}{2(\Lambda - k)} & \text{for} \quad k \geqslant \Lambda - 1 \\ (k + 1 - \pi/4)/\Lambda & \text{for} \quad k < \Lambda - 1. \end{cases} \tag{2.15}$$

2.3. *Final equations*

Based on the mass balance equation (2.4), the Bernoulli equation (2.5), the surface equation (2.12) and the cross-section (2.15) we obtain an unsteady, coupled, partial differential equation system of second order:

$$-\frac{\partial v}{\partial t} = -\frac{\partial h}{\partial x} + v\frac{\partial v}{\partial x} + \frac{K_f\,\tilde{l}}{2}\,v, \tag{2.16}$$

$$-\frac{\partial A}{\partial t} = v\frac{\partial A}{\partial x} + A\frac{\partial v}{\partial x}, \tag{2.17}$$

$$0 = \Gamma^2\,\frac{\partial^2 k}{\partial x^2} + \left(\frac{1}{R_1} - h\right)\left[1 + \Gamma^2\left(\frac{\partial k}{\partial x}\right)^2\right]^{3/2}, \tag{2.18}$$

$$0 = A(k) - \begin{cases} 1 - \dfrac{R^2}{2\Lambda}\arcsin\dfrac{1}{R} + \dfrac{1}{2\Lambda}(R - \Lambda + k), & k \geqslant \Lambda - 1, \\ \dfrac{1}{\Lambda}\left(k + 1 - \dfrac{\pi}{4}\right), & k < \Lambda - 1. \end{cases} \tag{2.19}$$

The boundary conditions are given by the unsteady pump flow rate at the channel outlet $v_1(t) = Q(t)/A_0$, the surface curvature at the inlet and the position of the liquid surface at the channel inlet and outlet (the surface is pinned at the edges of the closed ducts):

$$\left.\begin{aligned} v(x = 1) &= v_1(t) \\ h(x = 0) &= h_0 \\ k(x = 0) &= k(x = 1) = \Lambda \end{aligned}\right\}. \tag{2.20}$$

The surface curvature at the channel inlet h_0 strongly depends on the flow conditions in the tank and the nozzle, and on the interaction between the capillary channel and the compensation tube (streamlines A and B in figure 1(*b*)). It may be expressed with

$$-l_0\frac{\partial v_0}{\partial t} = -h_0 + K_0 + K_1\ \mathrm{Oh}\frac{v_0}{4} + K_2\frac{v_0^2}{2} + K_3\mathrm{Oh}\ [v_0 - v_1(t)]. \tag{2.21}$$

Unsteady flow causes a velocity difference between channel inlet and outlet $v_0 - v_1(t)$ and the liquid moves along streamline B in figure 1(*b*) with the pressure loss factor K_3. The factor K_0 is given by the system pressure, induced by the meniscus of the compensation tube in figure 1(*b*). The parameters K_1 and K_2 prescribe the pressure loss in the nozzle at the channel entrance. The frequency of the oscillation is mainly defined by the displaced liquid mass, represented by the effective length l_0 of streamline B. The parameter values are given in § 4.1.

2.4. *Numerical procedure*

For the numerical solution of the coupled nonlinear system (2.16)–(2.20) we treat v, A, h and k as variables and use finite differences and a uniform grid with $N \geqslant 1000$ discrete points. The derivatives $\partial_x v$, $\partial_x k$, $\partial_x h$ and $\partial_{xx} k$ are discretized by second-order central differences. At the inlet and outlet boundary, the derivatives are calculated by first-order upstream and downstream differences. In case of a steady solution the system of nonlinear equations is solved with a damped Newton method. Thus the time-dependent terms on the left-hand side of the system (2.16)–(2.20) are considered equal to zero. For time integration we apply the linearly implicit extrapolation code LIMEX (Ehrig *et al.* 1999). Combined with extrapolation this one-step method permits an adaptive step size and order control.

3. Open channel flow stability criteria

Equations (2.16)–(2.21) have been solved and compared to experimental data. The good agreement, as will be shown later, validates the model and allows one to formulate criteria for the stability of the flow. For the channel type examined, indicated by $\tilde{l} < 10^{-3}$ in the Oh and Λ range (§ 4.1), the irreversible pressure losses can be neglected (as shown by Rosendahl *et al.* 2004).

The liquid is confined to the open capillary channel by capillary forces only. These forces prevent leaking of the liquid and gas ingestion. The curvature of the liquid surface in figure 3(*a*) creates a capillary pressure h, prescribed by the Gauss–Laplace equation (2.12). The capillary pressure has to withstand all flow-induced pressure effects. One of them, the convective pressure χ, is caused by *convective acceleration* $v\partial v/\partial x$ in equation (2.16) due to cross-section changes in the flow direction. In the case of unsteady flow, the *local acceleration* $\partial v/\partial t$ in equation (2.16) adds an additional pressure effect, which is basically the difference $h - \chi$. Of major significance is the channel position x^* with the highest velocity and the minimum contour k^*, as shown in figure 3(*a*) (all variables identified with this point are denoted with an asterisk). The integral of equation (2.16) between channel positions $x = 0$ and $x = x^*$ is

$$\int_0^{x^*} \frac{\mathrm{d}v}{\mathrm{d}t}\mathrm{d}x = h^* - h_0^* - \tfrac{1}{2}\left(v^{*2} - v_0^2\right). \tag{3.1}$$

The irreversible pressure loss effects are of minor importance for the flow stability of this channel type and are neglected. Based on equation (3.1), the convective pressure

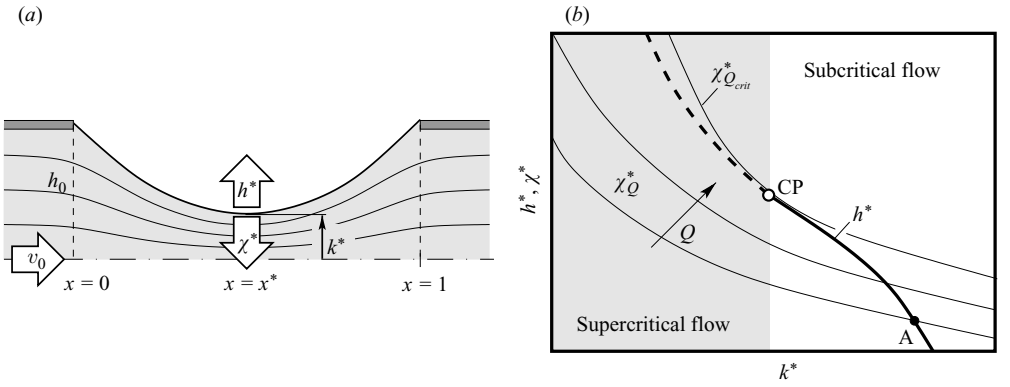

FIGURE 3. (*a*) Steady equilibrium of the capillary pressure h^* and the convective pressure χ^* at channel position x^*; v_0 is the entrance velocity, h_0 the entrance pressure. (*b*) Steady pressure diagram for the capillary pressure h^* (bold line) and the theoretical convective pressure k^*-dependence at different constant flow rates χ^*_Q (thin lines); k^* is the contour at $x = x^*$.

χ^* at the position $x = x^*$ in figure 3(*a*) can be defined as

$$\chi^* = h_0 + \tfrac{1}{2}\left(v^{*2} - v_0^2\right) . \tag{3.2}$$

The entrance pressure at $x = 0$ is h_0 (entrance curvature) and the entrance velocity is v_0. The convective pressure creates forces opposite to the capillary pressure h^*, as shown in figure 3(*a*). Furthermore, the convective pressure is a square function of the velocity v^* and increases significantly at a reduction of the cross-section and the contour k^*. Hence the convective pressure has a high potential for destabilization and plays a significant role in the liquid stability. Finally, the pressure balance at the channel position $x = x^*$ is

$$\int_0^{x^*} \frac{\mathrm{d}v}{\mathrm{d}t}\mathrm{d}x = h^* - \chi^* . \tag{3.3}$$

3.1. *Steady surface stability*

A special case is steady flow. The unsteady effect on the left-hand side of equation (3.3) is equal to zero. Hence, both pressures are in steady equilibrium $\chi^* = h^*$. The steady pressure diagram in figure 3(*b*) shows the dependence on the capillary pressure h^* on the surface contour k^* (bold line). The thin χ^*_Q-lines represent the theoretical behaviour of the convective pressure χ^* over k^* for a constant flow rate $Q = v^* A^*$. The cross-section $A^* = A(k^*)$ is defined by equation (2.19). A steady state is given by the intersection of the h^*-line and the χ^*_Q-line, e.g. at point A in figure 3(*b*) for a particular constant flow rate Q.

The stability of the equilibrium at point A is based on the higher gradient of the h^*-line in comparison to the χ^*_Q-line. An external perturbation (e.g. ambient pressure change) causes a surface movement, leading to (moderate) changes of k^*. The result is a change of the capillary pressure along the h^*-line and of the convective pressure along the χ^*_Q-line (due to the constant flow rate). Since the h^*-line is steeper than the χ^*_Q-line, the capillary pressure always acts in a stabilizing way and compensates the convective pressure. Hence a steady stability criterion can be formulated, based on the gradients:

$$\left|\frac{\partial h^*}{\partial k^*}\right| > \left|\frac{\partial \chi^*}{\partial k^*}\right| . \tag{3.4}$$

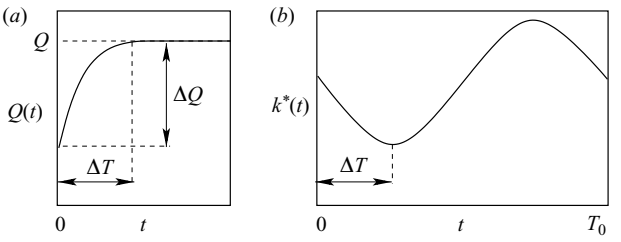

FIGURE 4. (*a*) The flow rate transition function $Q(t)$ is defined by a flow rate change ΔQ in a time period ΔT. The flow rate increases sinusoidally for $t < \Delta T$ and achieves a final, constant value of $Q(t) = Q$ at $t = \Delta T$. (*b*) The time period ΔT is defined as 1/4 of the natural period T_0. Thus the flow rate transition is in resonance with the natural frequency of the liquid oscillation.

Increasing the flow rate Q in small steps leads to a series of steady flow conditions. The surface bends inwards and the equilibrium point A in figure 3(*b*) moves upwards along the h^*-line. Owing to the power function of the velocity in the convective pressure equation (3.2), the gradient of the χ_Q^*-line increases significantly for smaller k values. On the other hand, the gradient of the h^*-line decreases slightly due to the geometrical constrictions of the bent liquid surface. It turns out that the difference of the gradients decreases with decreasing k^*. When a critical point CP in figure 3(*b*) is reached, the gradients are equal. The stability limit of the steady liquid flow is reached and the surfaces collapse. The stable equilibrium on the right-hand side of the critical point can be considered as subcritical.

At the critical point, a singularity occurs in the numerical solution. It can be shown that a supercritical numerical solution exists as well, marked by the dashed line in the grey area in figure 3(*b*). This is a theoretical state of no practical significance for the steady flow theory. But as shown below, it corresponds to the stability limit of unsteady flow.

Equating the terms of the inequality (3.4) and replacing the velocity by a small-amplitude wave speed v_{ca}^* leads to the capillary *speed index*, defined by Rosendahl *et al.* (2004):

$$S_{ca} = \frac{v^*}{v_{ca}^*} = v^* \sqrt{-\frac{1}{A^*}\frac{\partial A^*}{\partial h^*}}. \tag{3.5}$$

Each (small) flow rate change at the channel outlet requires an adjustment of the inlet flow rate. This causes a longitudinal disturbance, moving as a wave upstream with the wave speed v_{ca}. The wave velocity has to be higher than the flow velocity v^* to pass the point with the minimum cross-section. At the critical point CP in figure 3(*b*) the velocities are equal, $v_{ca}^* = v^*$, and the speed index reaches the value $S_{ca} = 1$; the channel is choked. In the case of further flow rate increase the free liquid surfaces collapse immediately and gas ingestion occurs.

3.2. *Unsteady surface stability*

For unsteady studies, a flow rate transition function $Q(t)$ is applied to emulate the pump dynamic. The transition function defines the velocity boundary condition $v_1(t) = Q(t)/A_0$ in equations (2.20) and (2.21). The function is based on experimental experience and performs a sinusoidal flow rate increase, as shown in figure 4(*a*). It is defined by the flow rate change ΔQ in a time period ΔT and the final constant flow

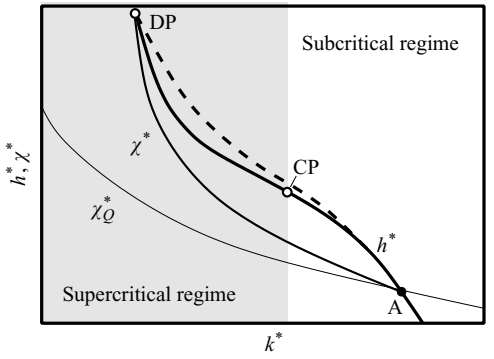

FIGURE 5. Unsteady pressure diagram for the capillary pressure h^* and the convective pressure χ^* for unstable flow. The dashed line represents the steady flow equilibrium, given in figure 3. The initial subcritical steady state is denoted A at the intersection of the h^*-line and the χ^*_Q-line. The supercritical regime is reached at the critical point CP. The surface collapse occurs at the destabilization point DP.

rate Q:

$$Q(t) = Q - \Delta Q \left(1 - \sin \frac{\pi t}{2\Delta T}\right), \quad 0 \leqslant t \leqslant \Delta T. \tag{3.6}$$

The transition function is $Q(t) = Q$ for $t > \Delta T$. The transition dynamic is defined as

$$\delta = \frac{\Delta Q}{\Delta T}. \tag{3.7}$$

The time period ΔT is defined as $1/4$ of the natural period T_0, as shown in figure 4(b). Thus the flow rate transition is in resonance with the natural frequency of the liquid oscillation. In the following the unsteady flow rate transition is defined by two parameters, the final flow rate Q and the preceding flow rate transition dynamic δ.

The flow rate transition increases the channel exit velocity v_1 of the boundary conditions (2.20). This causes acceleration pressure effects, defined by the time-dependent left-hand sides of equations (2.16), (2.21) and (3.3). The capillary pressure h^* and the convective pressure χ^* are not equal for a period of time as shown in the unsteady pressure diagram in figure 5. Point A indicates the subcritical steady state at the beginning of the unsteady phase. During the following transition the liquid surface is drawn into the channel and the contour k^* decreases. The capillary pressure h^* moves along the upper bold line of the pressure diagram in figure 5. The capillary pressure is a function of the liquid surface curvature only and thus behaves very similar to the steady case, as indicated by the dashed line, which matches the steady pressure diagram in figure 3(b). The difference between the steady and unsteady capillary pressure in figure 5 is based on surface deformations in the unsteady case. Liquid displacement from the vicinity of the channel outlet into the compensation tube causes surface asymmetry in the x-direction. The asymmetry has an influence on the surface curvature and the h^*-line is shifted to the left in comparison with the steady case.

The difference $h^* - \chi^*$ in figure 5 represents the dynamic pressure effect, caused by the acceleration term in equation (3.3). The χ^*-line increases to the left, below the h^*-line but above the χ^*_Q-line, owing to the increasing flow rate Q. Owing to the unsteady terms no singularity occurs for the numerical solution at the critical point CP. The flow remains stable and the supercritical flow regime on the left-hand side of the critical point in figure 5 can be reached in the case of dynamic flow.

Plate distance	$a = 10\,\text{mm}$
Plate width	$b = 25\,\text{mm}$
Channel length	$l = 15.4\,\text{mm}$ (12 mm)
Fluid density	$\rho = 1639\,\text{kg m}^{-3}$
Surface tension	$\sigma = 1.756 \times 10^{-2}\,\text{N m}^{-1}$
Viscosity	$\nu = 0.901 \times 10^{-6}\,\text{m}^2\,\text{s}^{-1}$

TABLE 2. Channel dimensions and liquid properties (HFE-7500; 15.8 °C), applied in the TEXUS 41 experiment.

The speed index (3.5) is a function of the geometrical properties A^* and h^* only and can be applied to the unsteady case as well. The speed index reaches the value $S_{ca} = 1$ at the critical point CP in figure 5 and the supercritical flow is choked. No further acceleration takes place and the distance $h^* - \chi^*$ decreases for decreasing k^* in the supercritical area. The communication between the channel outlet and inlet is interrupted. The inlet flow rate does not follow the outlet demand. The mismatch of the inlet and outlet flow rate in the choked channel is compensated by liquid displacement. The convective pressure increases significantly for decreasing k^* owing to the power law for the velocity in equation (3.2). The consequences are high local curvatures and a significant increase of the h^*-line gradient in the supercritical area.

When the (destabilizing) convective pressure χ^* reaches the value of the (conservative) capillary pressure h^*, the free liquid surfaces collapse at the destabilization point DP in figure 5. Hence the supercritical unsteady stability limit criterion can be formulated as

$$\chi^* < h^*. \tag{3.8}$$

If approached slowly, the unsteady stability limit is identical to the steady overcritical solution in figure 3(*b*); the destabilization point DP is on the dashed line in the supercritical regime in figure 5. Based on the unsteady stability limit, the *dynamic index*

$$D = 1 - \frac{h^* - \chi^*}{h^* - \chi_0^*} \tag{3.9}$$

is defined with the capillary pressure h^*, the convective pressure χ^* and the convective pressure at the beginning of the unsteady phase $\chi_0^* = \chi^*(t = 0)$ (point A in figure 5). The initial value $h^* - \chi_0^*$ serves for scaling and to suppress false indication at $t = 0$ in the subcritical area. The difference $h^* - \chi^*$ tends to zero at the stability limit. An unsteady open capillary channel flow is stable if the dynamic index does not reaches the value $D = 1$ in the supercritical area.

4. Experimental and numerical results

4.1. *Experimental verification of the model*

The model was verified by comparison to results of a sounding rocket experiment on capillary channel flow (TEXUS 41), launched from ESRANGE in north Sweden in December 2005 (Rosendahl & Dreyer 2007). The geometric properties of the channel are depicted in figure 1(*a*), the experimental set-up is shown in figure 1(*b*). The test liquid used for the experiment is HFE-7500. Channel dimensions and liquid properties are given in table 2.

The scaling is performed according to the definitions in table 1. The scaled model parameters and characteristic numbers for the numerical evaluation are given in

Parameter	Value	Equation
Dimensionless length	$\tilde{l} = 7.5 \times 10^{-4}$	(2.1)
Ohnesorge number	$Oh = 1.95 \times 10^{-3}$	(2.2)
Aspect ratio	$\Lambda = 2.5$	(2.3)
Pressure loss factor	$K_{pf} = 96$	(2.9)
Entrance factor	$L = -208$	(2.11)
Inlet factor	$K_0 = 0.333$	(2.21)
Inlet factor	$K_1 = 498$	(2.21)
Inlet factor	$K_2 = 1.4$	(2.21)
Inlet factor	$K_3 = Oh^{-1}$	(2.21)
Effective streamline length	$l_0 = 12.5$	(2.21)

TABLE 3. Scaled parameter values for numerical evaluation.

table 3. The channel length l, the aspect ratio Λ, and the Ohnesorge number Oh are defined by geometry and liquid properties in table 2. Owing to wetting problems during the experiment the liquid surface did not remain pinned to the channel inlet. The contact line of the surface moved upwards along the housing and the free surface length increased. An effective surface length of $l = 15.4$ mm is measured.

The pressure loss factor for parallel plates K_{pf} is derived from White (1986). The factor $K_0 = (p_a - p)a/(2\sigma)$ represents the capillary pressure, induced by the meniscus in the compensation tube. The entrance factor L and the inlet factors K_1 and K_2 are based on three-dimensional evaluations using commercial software for the inlet nozzle in figure 1(*b*). The parameters for unsteady liquid movement along streamline B in figure 1(*b*) are the inlet factor K_3 and the effective streamline length l_0. K_3 is the effective pressure loss factor for the displacement flow from the channel into the compensation tube (and back) and was approximated with a circular tube flow. The effective streamline length l_0 represents the physical distance between the capillary channel and the compensation tube. It was particularly difficult to obtain precise values for K_3 and l_0 owing to the complicated set-up geometry, which was primarily designed for steady flow observation. Thus, the theoretically obtained values had to be adapted to the set-up, based on observation of frequency, amplitude, and damping of the liquid oscillation. However, the adaptation of the inlet factors has no influence on the results of the surface stability analysis for the present geometry.

A comparison of scaled experimental and numerical results is shown in figure 6. The upper diagram in figure 6(*a*) shows the surface contour k^* (at the point of minimum cross-section) over time t. The lower diagram in figure 6(*a*) shows the actual flow rate $Q(t)$ measured in the experiment. It was used to define the outlet flow velocity $v_1(t)$ of the boundary conditions (2.20) and (2.21) of the model. The surface oscillations are a result of the stepwise increase of the flow rate of the pump. The numerical solutions over time in figure 6(*a*) and the corresponding profiles over the channel length in figure 6(*b*) are in good agreement with the experimental results.

4.2. *Steady flow stability studies*

To examine the stability limits of the TEXUS 41 liquid surface system, the theory described in § 3 is applied onto the model in § 2. The pressure diagram for steady flow is shown in figure 7. It corresponds to the principle explained in figure 3(*b*).

The bold line represents the capillary pressure h^* at the point of minimum cross-section. The thin χ^*_Q-lines show the convective pressure χ^* as a theoretical function of the surface position k^* for different constant volume flow rates Q. The convective

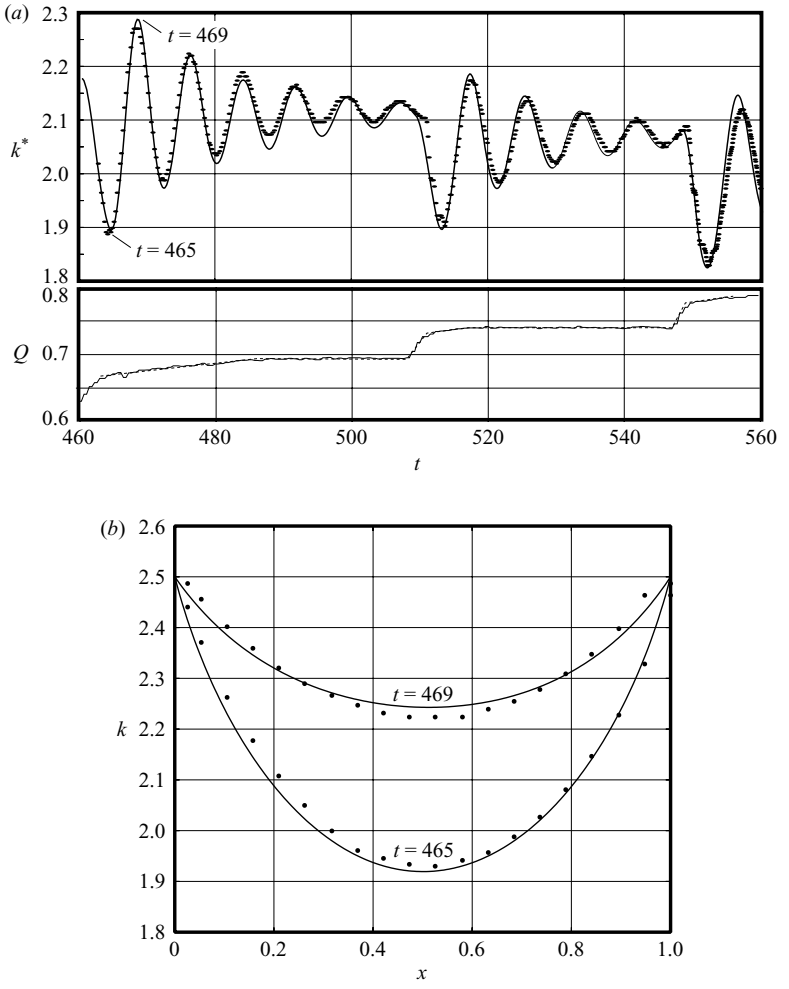

FIGURE 6. Comparison of numerical (—) and experimental (· · ·) liquid surface contour for the TEXUS 41 experiment: (*a*) oscillation of the contour k^* versus time t (the asterisk denotes quantities at the point of minimum contour along the channel length x); Q is the measured flow rate; (*b*) contour k over the channel length x at selected time points.

pressure is defined by equation (3.2). The bottom χ_Q^*-line in case of no flow ($Q = 0$) represents the remaining system pressure $K_0 = 0.333$ (table 3) induced by the meniscus in the compensation tube in figure 1(*b*).

In general the actual steady pressure equilibrium $h^* = \chi^*$ is defined by the intersection of the h^*-line and the χ_Q^*-line for a specified flow rate Q. The critical point CP divides the h^*-line into two flow regimes. The subcritical flow regime is indicated with a bold h^*-line, the supercritical flow regime with a dashed bold line (grey area). In the subcritical area the h^*-line is steeper than the χ_Q^*-lines and the liquid surface is stable because of the subcritical criterion (3.4). The speed index (3.5) is less than unity in this area. The critical point CP is located where the gradients of the h^*-line and one of the χ_Q^*-lines are equal and the speed index attains unity. The corresponding flow rate is the critical flow rate Q_{crit}, which causes a liquid surface collapse for steady flow. In the supercritical regime the χ_Q^*-lines are steeper and no steady flow

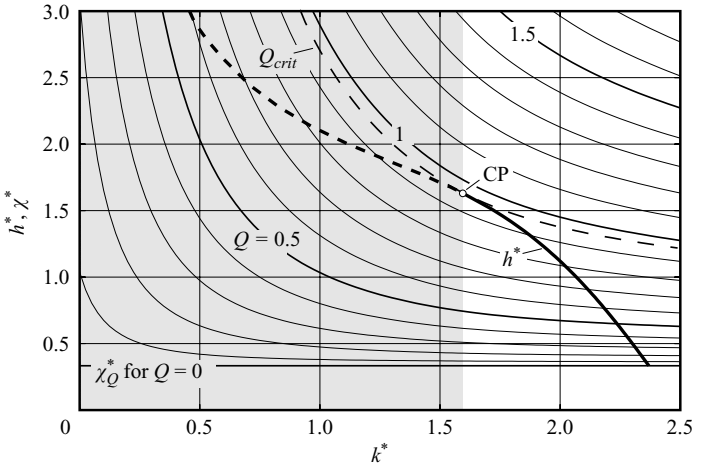

FIGURE 7. Steady pressure diagram for the TEXUS 41 experiment (numerical evaluation). The bold line is the capillary pressure h^*, the thin lines represent the theoretical convective pressure as a function of the contour k^* for different flow rates Q. The critical flow rate is $Q_{crit} \approx 0.946$.

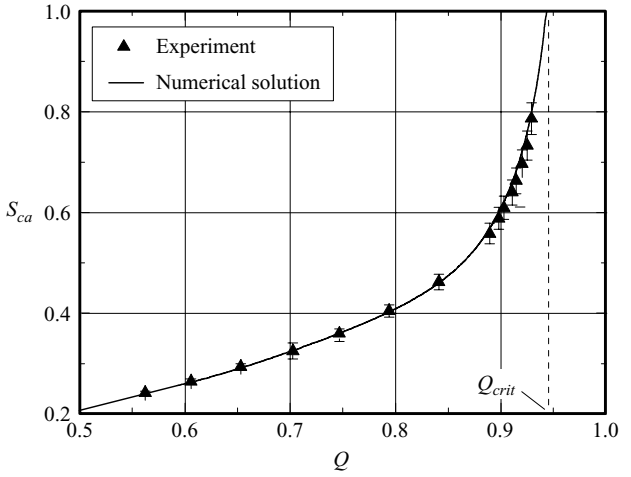

FIGURE 8. Comparison of numerical and experimental steady speed index values S_{ca} over the flow rate Q (TEXUS 41). The critical flow rate is $Q_{crit} \approx 0.946$.

is possible. The supercritical solution has no significance for steady flow, but defines the dynamic stability limit for unsteady flow. The numerically evaluated critical flow rate is $Q_{crit} \approx 0.946$. As shown in figure 8 the highest achieved experimental flow rate was $Q \approx 0.93$. Owing to the high sensitivity at this flow rate, very small perturbations normally cause early collapse of the surfaces. The unperturbed experimental critical flow rate can be assumed slightly higher, which matches well the numerical value. The geometry of the channel and the symmetry of the liquid surfaces in the represented case allow an estimation of the capillary pressure at the critical point;

$$h^*_{\mathrm{CP}} \approx \left(\frac{1}{R_1} + \frac{1}{R_2}\right) = 1 + \frac{a}{l} = 1.65, \tag{4.1}$$

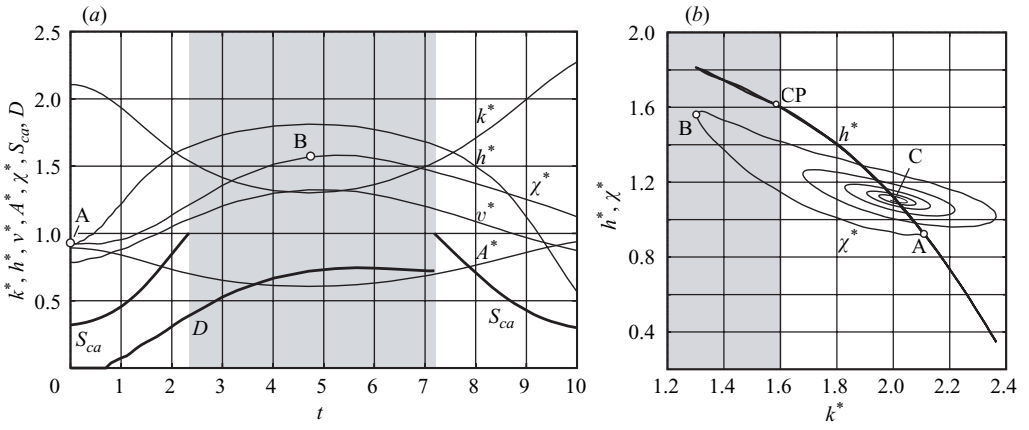

FIGURE 9. Stable oscillation for a transition dynamic $\delta = 0.05$ and a final flow rate $Q = 0.8$. (*a*) First amplitude with the speed index and dynamic index vs. time. (*b*) Pressure diagram for the entire oscillation: A, initial steady state; B, supercritical amplitude; C, final steady state.

using the Gauss–Laplace equation (2.12). The radii are approximately $R_1' \approx a/2$ and $R_2' \approx l/2$ at the point of maximum curvature. The scaled radii are $R_1 = 1$ and $R_2 = a/l$ (scaled with $a/2$, according to table 1). Plate distance a and channel length l are given in table 2. The value $h_{CP}^* \approx 1.65$ matches well the capillary pressure at the critical point CP in figure 7.

The comparison of evaluated and experimental subcritical steady speed index values is shown in figure 8. The experimental measurement was performed according to the method represented by Rosendahl *et al.* (2004).

4.3. *Unsteady flow stability studies*

For unsteady flow stability studies the flow rate function for the pump dynamic given in equation (3.6) is applied. The flow transition is defined by the final constant flow rate Q and the dynamic $\delta = \Delta Q/\Delta T$, given in equation (3.7). The time constant ΔT is defined as 1/4 of the natural time period of the oscillation. For the TEXUS 41 system the time constant could be approximated by $\Delta T = 2$, based on observation of the oscillation in figure 6.

A stable oscillation caused by a flow rate transition is shown in figure 9. The transition dynamic is $\delta = 0.05$ and the final flow rate after the transition is $Q = 0.8$. The first oscillation amplitude over time is depicted in figure 9(*a*) for the solution of equations (2.16)–(2.19). The model variables are the surface contour k^*, the capillary pressure (surface curvature) h^*, the flow velocity v^* and the cross-section A^*. Furthermore the convective pressure χ^* (3.2), the speed index S_{ca} (3.5) and the dynamic index D (3.9) versus time are shown.

The initial state at $t = 0$ is steady flow in the subcritical regime. The capillary pressure and the convective pressure are in balance at point A. The transition phase starts with the flow rate acceleration. As the liquid surfaces are drawn into the channel, the contour k^* and the cross-section A^* decrease. The capillary pressure h^*, the velocity v^* and the convective pressure χ^* increase. The speed index S_{ca} and the dynamic Index D increase as well. The convective pressure maximum is reached at point B.

The supercritical regime (grey) is reached, when the speed index reaches unity in figure 9(*a*). The capillary wave speed is smaller than the flow velocity and the channel

is choked. The communication between the pump at the channel outlet and the inlet is temporarily interrupted in the area of minimum cross-section. The channel inlet flow does not follow the outlet acceleration and the transportation mismatch is compensated by liquid displacement between the channel and the compensation tube. The convective pressure χ^* remains below the value of the capillary pressure h^* during the supercritical phase. Hence, the dynamic index D remains below the critical value 1 and the unsteady flow is stable.

In the pressure diagram in figure 9(b) the entire damped oscillation is shown for the capillary pressure h^* and the convective pressure χ^* as functions of the contour k^*. The initial steady pressure equilibrium at point A and the first convective pressure amplitude at point B correspond with figure 9(a). The supercritical regime is reached at the critical point CP, which is a turning point on the h^*-line. At point C the capillary pressure h^* and the convective pressure χ^* are in steady equilibrium again. Contrary to the unstable pressure diagram in figure 5 the convective pressure remains below the capillary pressure and the unsteady flow is stable in this case.

In order to give an overview of the unsteady flow stability for this channel type, numerical studies are performed for different transition dynamics and different flow rates. The subcritical unsteady speed index diagram is shown in figure 10(a). The flow rate Q is the final flow rate after the transition defined by equation (3.6), and S_{ca} is the maximal speed index value during the transition (example: a transition to a final flow rate of $Q = 0.6$ with a dynamic $\delta = 0.05$ produces temporarily a maximal speed index value of $S_{ca} \approx 0.59$). The bottom line represents the speed index for steady flow $\delta = 0$ and corresponds to the steady function in figure 8. The critical flow rate for the steady flow is $Q_{crit} \approx 0.946$ where the speed index reaches the value $S_{ca} = 1$ and the liquid surfaces collapse. For increasing dynamics δ the speed index line is shifted to the left and the flow rate at which unity is reached decreases.

The transition diagram in figure 10(b) gives an overview of steady and dynamic flow stability for the present channel type. The diagram is based on numerical evaluations. The symbols are actual stable (filled symbols) and unstable (open symbols) transitions observed in the TEXUS 41 experiment. The speed index S_{ca}, the maximum dynamic index D and the available flow regimes are shown as functions of the flow rate Q (after the transition) and the transition dynamic δ. Subcritical flow can be found in area A ($S_{ca} < 1$), supercritical stable flow in area B ($S_{ca} > 1$, $D < 1$) and subcritical unstable flow in area C ($D > 1$). At $S_{ca} = 1$ the flow rate reaches the critical value $Q = Q_{crit}$ and the flow is temporarily choked, but remains stable. At the stability limit $D = 1$ the flow rate reaches the maximal value $Q = Q_{max}$ for stable flow. Further increase of the flow rate or the transition dynamic will cause liquid surface collapse. For example, the transition to $Q = 0.4$ with $\delta = 0.05$ yields $S_{ca} \approx 0.3$ which is obviously subcritical and the transition to $Q = 0.8$ with $\delta = 0.05$ is supercritical and stable. The maximal possible stable flow rate for the transition dynamic $\delta = 0.05$ is $Q_{max} \approx 0.83$. For the steady case, which can be found on the abscissa ($\delta = 0$), the maximum flow rate is identical to the critical flow rate $Q_{max} = Q_{crit} \approx 0.946$ (figures 7 and 8) at the point $D = S_{ca} = 1$. A steady stable supercritical flow regime does not exist. The dashed line in both diagrams in figure 10 is based on the fact that a flow rate cannot be less than the preceding flow rate increase.

In figure 11 a numerical parameter study for the TEXUS 41 channel geometry is shown. The investigated parameter is the scaled channel length $\tilde{l}$. The diagram displays the maximum flow rate Q_{max} over the transition dynamic δ. The maximum flow rate is the highest value for the flow rate Q in equation (3.6) that does not lead

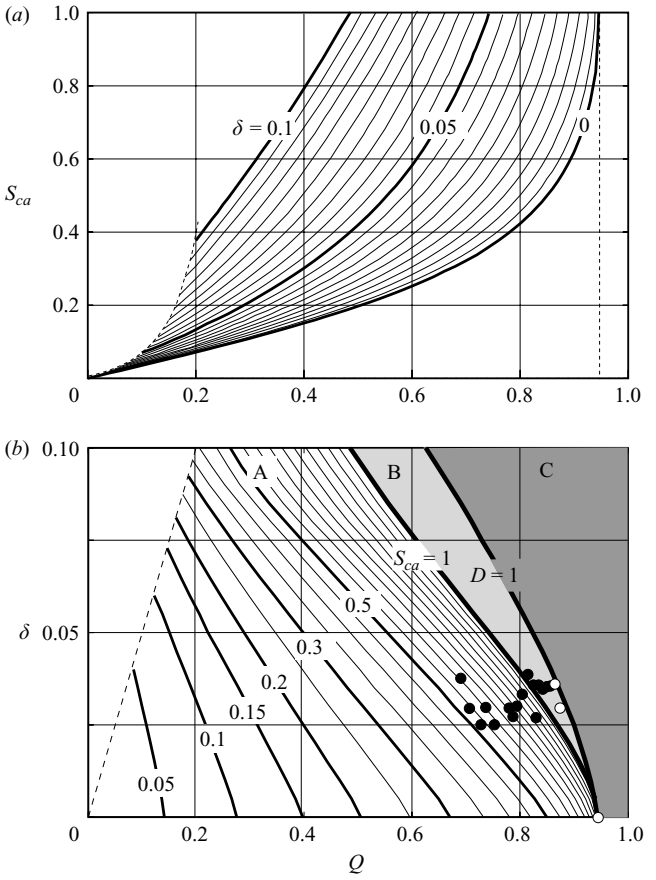

FIGURE 10. (*a*) Speed index S_{ca} vs. flow rate Q for different transition dynamics δ. (*b*) Transition dynamic δ vs. flow rate Q with subcritical regime A, supercritical regime B and unstable flow regime C. The demarcation line for the supercritical regime is $S_{ca} = 1$, the stability limit is $D = 1$. The symbols denote stable (filled) and unstable (open) transitions in the TEXUS 41 experiment. In (*a*) and (*b*) the limit on the left (dashed line), a final flow rate cannot be less than the preceding flow rate increase. The critical flow rate for the steady flow is $Q_{crit} \approx 0.946$.

to a collapse of the free liquid surfaces. The parameter value valid for the TEXUS 41 experiment geometry is denoted by the dashed line in figure 11. In general, the maximum flow rate decreases for higher transition dynamics δ. The increase of the scaled channel length $\tilde{l}$ causes an increase of the viscous pressure loss effect and the maximum flow rate is decreasing. The available transition dynamic on the other hand is increasing with increasing channel length $\tilde{l}$ in the plotted parameter range. This effect is based on an increasing amount of liquid within the channel and thus a diminishing sensitivity for temporary mismatch between outlet and inlet flow rates in the case of choking.

5. Summary

This paper investigates steady and unsteady forced liquid flow through an open capillary channel under low-gravity conditions. The channel is bounded by free liquid surfaces at the open sides. Based on experimental observation a one-dimensional

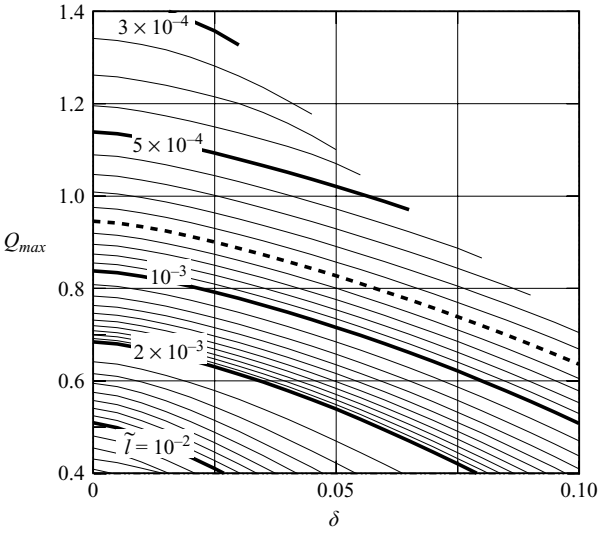

FIGURE 11. The maximum flow rate Q_{max} as a function of the transition dynamic δ and the scaled channel length $\tilde{l}$; the dashed line represents the maximum flow rate for the TEXUS 41 experiment geometry ($\tilde{l} = 7.5 \times 10^{-4}$).

unsteady flow model is formulated and applied for numerical studies. The model is related to the capillary pressure at the free surface and the convective pressure caused by spatial liquid velocity change. Experiments performed aboard a sounding rocket are presented and show good agreement with the numerical calculations.

The investigation is focused on the effect of flow rate limitation for both steady and unsteady flows. If the flow rate exceeds a certain limit the free surfaces of the channel collapse. The formulations of the stability criteria are based on the relation of the capillary pressure and the convective pressure. The capillary pressure acts to stabilize, but the convective pressure acts in the opposite way.

The stability criterion for steady flow is based on a higher gradient of the capillary pressure in comparison to the gradient of the convective pressure. The criterion defines a critical point where the gradients are equal and the surfaces collapse. The critical point corresponds to the maximum flow rate. Steady flow is possible only in the subcritical area below the critical point. The steady stability condition can be related to the speed index S_{ca}.

Unsteady flow yields an additional decrease of the flow rate limit due to acceleration flow effects. The critical point does not represent the stability limit but defines the change to supercritical flow. Supercritical flow is a choked flow when the speed index reaches unity and the stability is based on a higher capillary pressure in comparison to the convective pressure. A dynamic index D is defined that is valid in the supercritical area. The surfaces collapse when the index reaches unity.

Numerical parameter studies are performed to identify the three regions in which the unsteady flow is subcritical, supercritical, or unstable. The governing parameters are the flow rate transition dynamic and the final flow rate. The result is a stability diagram which classifies stable and instable flow conditions for a channel. Comparison to stable and unstable flow rate transitions in the TEXUS 41 experiment shows good agreement to the predictions.

The funding of the sounding rocket flight and the research project by the German Ministry of Education and Research (BMBF) through the German Aerospace Center (DLR) under grant numbers 50WM0421 and 50WM0535 is gratefully acknowledged.

REFERENCES

Ehrig, R., Nowak, U., Oeverdieck, L. & Deuflhard, P. 1999 Advanced extrapolation methods for large scale differential algebraic problems. In *High Performance Scientific and Engineering Computing*. Lecture Notes in Computational Science and Engineering, vol. 8 (ed. H.-J. Bungartz, F. Durst & C. Zenger), pp. 233–244. Springer.

Jaekle Jr., D. E. 1991 Propellant management device conceptual design and analysis: Vanes. *AIAA Paper* 91-2172, pp. 1–13.

Landau, L. D. & Lifschitz, E. M. 1959 *Fluid Mechanics*, *Course of Theoretical Physics*, vol. 6. Pergamon.

Rosendahl, U. 2007 *Über die Grenzen des stationären Flüssigkeitstransportes in offenen Kapillarkanälen*. Cuvillier Verlag Göttingen.

Rosendahl, U. & Dreyer, M. E. 2007 Design and performance of an experiment for the investigation of open capillary channel flows. *Exps. Fluids* **42**, 683–696.

Rosendahl, U., Ohlhoff, A. & Dreyer, M. E. 2004 Choked flows in open capillary channels: theory, experiment and computations. *J. Fluid Mech.* **518**, 187–214.

Sparrow, E. M. & Lin, S. H. 1964 Flow development in the hydrodynamic entrance region of tubes and ducts. *Phys. Fluids* **7**, 338–347.

Srinivasan, R. 2003 Estimating zero-g flow rates in open channels having capillary pumped vanes. *Intl J. Numer. Meth. Fluids* **41**, 389–417.

White, F. 1986 *Fluid Mechanics*. McGraw Hill.